Model Based Segmentation of Nuclei

Ge Cong and Bahram Parvin

Information and Computing Sciences Division
Lawrence Berkeley National Laboratory
Berkeley, CA 94720
www-itg.lbl.gov/VISION

Abstract

A new approach for segmentation of nuclei observed with an epi-fluorescence microscope is presented. The technique is model based and uses local feature activities such as step-edge segments, roof-edge segments, and concave corners to construct a set of initial hypotheses. These local-feature activities are extracted using either local or global operators to form a possible set of hypotheses. Each hypothesis is expressed as a hyperquadric for better stability, compactness, and error handling. The search space is expressed as an assignment matrix with an appropriate cost function to ensure local, adjacency, and global consistency. Each possible configuration of a set of nuclei defines a path, and the path with the least error corresponds to best representation. This result is then presented to an operator who verifies and eliminates a small number of errors.

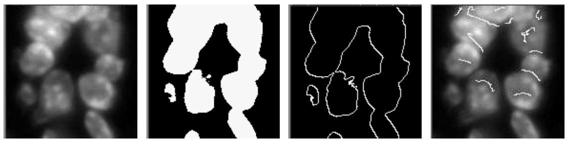

(a) (b) (c) (d)

Figure 1: An example of nuclei with the results of global and local operations: (a) original image; (b) threshold image; (c) boundary objects; and (d) local troughs.

1 Introduction

Automatic delineation of nuclei in cells is an important step in mapping functional activities into structural components of cell biology. This paper examines delineation of individual nucleus that are observed with an epi-fluorescence microscope. The target nuclei belong to epithelial cells that are the basic building blocks for milk-carrying capillaries in the breast tissue. The intent is to build the necessary computational tools for large scale population studies and hypothesis testing. These nuclei are usually clumped together, thus making quick delineation nearly impossible. Our original data set is obtained in 3D through a confocal microscope. In this paper, we focus on what can be accomplished by just analyzing one slice at a time. An example is shown in Figure 1, where a single layer of nuclei enclose the capillary (the dark hole in the middle). The figure also indicates that simple thresholding is not sufficient for delineating individual nucleus. Previous efforts in this area have been focused on thresholding, local geometries, and morphological operators for known cell size [14, 16]. Others have focused on an "Optimal Cut Path" that minimizes a cost function in the absence of shape, size, or other information [6, 10, 7, 4, 19].

In this paper, we extract partial information corresponding to step and roof edges and then group them through geometric reasoning. The intent is to construct a partitioning that is globally consistent. A list of step edges is constructed by thresholding raw images, recovering corresponding boundaries, and localizing concave corners from their polygonal approximation. These corners provide possible cues to where two adjacent nuclei may touch each other. Thresholding separates big clumps consisting of several nuclei squeezed together, but the boundaries between adjacent nuclei cannot be detected since they have higher intensities. However, the partial boundaries between adjacent nuclei can be recovered by extracting crease segments [8, 9, 18, 17], as shown in Figure 1(d). These crease segments correspond to trough edges (positive curvature maxima), but false creases may also be extracted in the process. Nevertheless, dealing with noise and erroneous segments is a higher-level process that is handled during the grouping process. Our system generates a number of hypotheses for possible grouping of the boundary segments. A unique feature of this system is in hyperquadric representation of each hypothesis and the use of this representation for global consistency. The main advantage of such a parameterized representation (as opposed to polygonal representation) is compactness and better stability in shape description from partial information. In this fashion, each step-edge boundary segment belongs to one and only one nucleus while each roof-edge boundary segment is shared by two and only two nuclei. These initial hypotheses and their localized inter-relationship provides the basis for search in the grouping step. This is expressed in terms of an adequate cost function and minimized through dynamic programming. The final result of this computational step is then shown to an operator for verification and elimination of false alarms.

In the next section, we will briefly review each step of the representation process and parameterization of each hypothesis in terms of hyperquadric. This will be followed by the details of the grouping protocol, results on real data,

*This work is supported by the Director, Office of Energy Research, Office of Computation and Technology Research, Mathematical, Information, and Computational Sciences Division, and Office of Biological and Enviornmental Research of the U. S. Department of Energy under contract No. DE-AC03-76SF00098 with the University of California. The LBNL publication number is 43106.

and concluding remarks.

2 Representation

The initial step of the computational process is to collect sufficient cues from local feature activities so that a set of hypotheses–not all of them correct–can be constructed for consistent global grouping. These initial steps include thresholding, detection of concave points from boundary segments, extraction of crease segments from images, and hyperquadric representation of each possible hypothesis.

2.1 Thresholding

Binary thresholding can extract the clump patterns from the original image. The corresponding threshold is obtained either through analysis of the intensity histogram or contrast histogram. In the contrast analysis, desirable threshold corresponds to the peak in the contrast histogram that is the accumulation of the local contrast information at each edge point. Thresholding is a valid step for some applications of fluorescence image analysis. It has to do with the absence of shading and uniform response of microanatomy to fluorescence material.

2.2 Polygonal approximation

This step partitions the clump silhouettes into segments that correspond to partial nucleus boundaries. Often the boundary location between two adjacent nuclei is signaled by a concave corner. These corners can be localized by the concave vertices of the polygonal approximation to the original contours. Concavity is then determined by the turning angle between adjacent line segments. An example of this step of the process is shown in Figure 2.

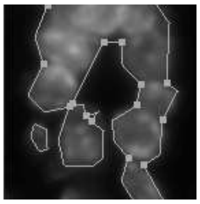

Figure 2: Detection of concave corners

2.3 Detection of crease boundaries

This step detects the common boundaries between adjacent nuclei in a cluster of cells. In grey images, crease points can be defined as local extremes of the principal curvature along the principal direction [8, 9, 18, 17]. It is well known that as a result of noise, scale, finite differential operators, and thresholds, it is very difficult to detect complete creases as shown in Figure 1(d). Images are enhanced through a variation of nonlinear diffusion [13] to improve localization of crease points. The principal curvature k is then computed as the solution of the following equation [15]:

$$(EG-F^2)k^2-(EN+GL-2FM)k+(LN-M^2)=0 \quad (1)$$

where E, F, G, L, M, N are the $1st$ and $2nd$ fundamental forms. The principal direction $(dx : dy)$ is given by the following equation [15]

$$(EM-LF)dx^2+(EN-LG)dxdy+(FN-MG)dy^2=0 \quad (2)$$

Crease points are detected and linked to form "crease segments" as shown in Figure 1(d).

2.4 Hyperquadric model

A brief introduction to hyperquadric fitting is included. (A more detailed description can be found in references[2, 3, 5]). A 2D hyperquadric is a closed curve defined by:

$$\sum_{i=1}^{N} |A_i x + B_i y + C_i|^{\gamma_i} = 1 \quad (3)$$

Since $\gamma_i > 0$, (3) implies that

$$|A_i x + B_i y + C_i| \leq 1 \quad \forall i = 1, 2, ..., N \quad (4)$$

Equation 4 defines a pair of parallel line segments for each i. These line segments define a convex polytope (for large γ) where the hyperquadric is constrained to lie. This representation is valid across a broad range of geometrical shapes, which unlike superquadric may not need to be symmetric. The parameters A_i and B_i determine the slopes of the bounding lines and, along with C_i, the distance between them. γ_i determines the "squareness" of the shape. Hyperquadric can model both convex and concave shapes.

2.4.1 Fitting problem

Let points $p_j = (x_j, y_j), j = 1, 2, ..., m$ from n segments $(m = \sum_{i=1}^{n} m_i)$ be given. The fitting cost function is defined as:

$$\epsilon^2 = \sum_{j=1}^{m} \frac{1}{||\nabla F_j(p_j)||^2}(1 - F_j(p_j))^2 + \lambda \sum_{i=1}^{N} Q_i \quad (5)$$

where $F_j(p_j) = \sum_{i=1}^{N} |A_i x_j + B_i y_j + C_i|^{\gamma_i}$, ∇ is the gradient operator, λ is the regularization parameter, and Q_i is the constraint term [5]. The parameters A_i, B_i, C_i, γ_i are calculated by minimizing ϵ, using the Levenberg-Marquard nonlinear optimization method [11] from a suitable initial guess [5]. Several examples of hyperquadric fitting to an initial set of partial segments are shown in Figure 3.

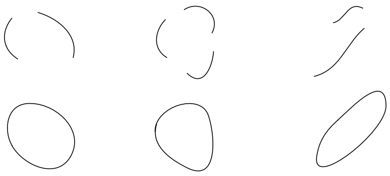

Figure 3: Fitting results for hyperquadrics.

3 Grouping of nuclei

Let each clump be represented by n_b boundary segments $b_i, i = 1, ..., n_b$ and n_c crease segments $c_i, i = 1, ..., n_c$. We assume that there are at most n_b nuclei in a cluster clump. Hypothesis Φ_i consists of a set of boundary and crease segments belonging to the ith nucleus. Note that Φ_i does not necessarily include b_i and may be empty. All segments on the target Φ_i are fitted by a hyperquadric as the actual shape of the nucleus. To delineate each nucleus of a clump, we need to find a consistent partition of $b_i, i = 1, ..., n_b$ and $c_i, i = 1, ..., n_c$ into $\Phi_i, i = 1, ..., n_b$. Each b_i belongs to one and only one Φ_i, while each c_i belongs to two different nuclei (common boundary) or not a single nucleus (false crease). This is called the consistence criterion. Thus, two or more boundary segments may be assigned to the same Φ_i, while some other Φ_i are unfilled.

To assign the segments, we define a new set $\tilde{\Phi}_i$ for each Φ_i such that $\Phi_i \subseteq \tilde{\Phi}_i$. It is assumed that detecting $\tilde{\Phi}_i$ is trivial and $\tilde{\Phi}_i$ contains all the segments that have certain possibilities to be part of the ith nucleus. Computing Φ_i from $\tilde{\Phi}_i$ is in fact subject to local, adjacency, and global constraint. It is under-constrained and the solution is not unique. Each possible solution is measured by the "goodness criteria" proposed in Section 3.3, the one with minimum cost determines the segmentation.

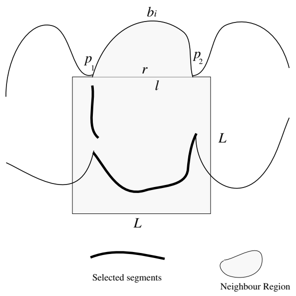

Figure 4: Neighborhood function

3.1 Neighborhood function

A neighborhood function is defined over a region for each b_i for construction of $\tilde{\Phi}_i$, as shown in Figure 4. Suppose that p_1 and p_2 are the end points of b_i and r is the line segment connecting them with $l = ||r||$ as the length. The neighborhood function is then defined as the combination of a square that extends r and the region enclosed by b_i. The length of the square edge is a pre-set number L unless $l > L$ where the length is set to l.

Any segment b_j or c_j that resides in the target rectangle is included in $\tilde{\Phi}_i$. If L is properly selected then all boundary and crease segments of Φ_i are guaranteed to be in the target region, e.g. $\Phi_i \subseteq \tilde{\Phi}_i$.

3.2 Search strategy

The next step is to compute Φ_i from $\tilde{\Phi}_i$ subject to a consistency criterion. Since every segment in $\tilde{\Phi}_i$ has some possibility to be in Φ_i, the solution is not unique. However, the construction of $\tilde{\Phi}_i$ reduces the search space greatly. The optimal segmentation is computed by enforcing local, adjacency, and global criterion. The key data structure in our approach is the *Assignment Matrix* $\mathcal{M}$. Each row of $\mathcal{M}$ indicates a possible nucleus. For the clump under investigation, we can construct up to n_b nuclei. Thus, $\mathcal{M}$ has n_b rows. Each column of $\mathcal{M}$ indicates a boundary or crease segment. Since each crease may be shared by two nuclei, two columns are assigned to it. Hence, $\mathcal{M}$ has $n_b + 2n_c$ columns. Let

$$\begin{aligned} s_j &= b_j, \quad 1 \le j \le n_b \\ s_{n_b+2j-1} &= s_{n_b+2j} = c_j, \quad 1 \le j \le n_c \end{aligned} \tag{6}$$

$\mathcal{M}$ is determined by

$$m_{ij} = \begin{cases} 1 & \text{if } s_j \in \tilde{\Phi}_i \\ 0 & \text{otherwise} \end{cases} \tag{7}$$

An example for construction of $\mathcal{M}$ for feature segments of Figure 5 is shown in Figure 6, where we assume that

$$\begin{aligned} \tilde{\Phi}_1 &= \{b_1, c_1, b_4, b_5\} \\ \tilde{\Phi}_2 &= \{b_2, c_1, b_5, b_6\} \\ \tilde{\Phi}_3 &= \{b_3, b_6\} \\ \tilde{\Phi}_4 &= \{b_4, c_1, b_1\} \\ \tilde{\Phi}_5 &= \{b_5, c_1, b_2\} \\ \tilde{\Phi}_6 &= \{b_6, b_3\} \end{aligned} \tag{8}$$

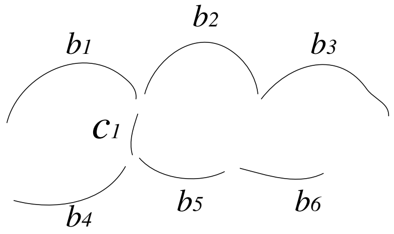

Figure 5: An example of boundary and crease segments

	s_1	s_2	s_3	s_4	s_5	s_6	s_7	s_8
nucleus 1	1	0	0	1	1	0	1	1
nucleus 2	0	1	0	0	1	1	1	1
nuclues 3	0	0	1	0	0	1	0	0
nucleus 4	1	0	0	1	0	0	1	1
nucleus 5	0	1	0	0	1	0	1	1
nucleus 6	0	0	1	0	0	1	0	0

Path I
Path II

Figure 6: Assignment matrix for features of Figure 5

The ith row of $\mathcal{M}$ represents all possible segments that may be part of a nucleus. The jth column of $\mathcal{M}$ indicates all possible nuclei that s_j may belong to. The main constraint is to assign a boundary segment in one and only one nucleus and to share a crease segment between only two different nuclei (or not using this segment at all for any nucleus). According to this consistency criterion, a "path" in $\mathcal{M}$ is defined as a routine from left to right with the so-called "boundary part" and "crease part." The boundary part passes one and only one "1" for each boundary column. For each pair of crease columns, s_{n_b+2j-1} and s_{n_b+2j}, the crease part passes either one "1" in each column but different rows or does not pass any "1" in the two columns at all. Thus, each path is a segmentation of the clump with assignments of Φ_i. In each path, every boundary segment is assigned to a nucleus while some crease segments may not be used at all. For example, Path I in figure 6 indicates that

$$\begin{aligned} \Phi_1 &= \{b_1\} \\ \Phi_2 &= \{b_2, c_1, b_5\} \\ \Phi_3 &= \{b_3, b_6\} \\ \Phi_4 &= \{b_4\} \\ \Phi_5 &= \{c_1\} \\ \Phi_6 &= \phi \end{aligned} \tag{9}$$

$\Phi_i, i = 1,2...$ are then fitted by hyperquadrics each of which is evaluated by the criteria proposed in the next section. Segmentation problem then reduces to finding a partition among competing hypotheses such than no partition shares a boundary segment with other patitions and crease segments can be shared at most by two partitions. For example, the best partition for Figure 5 is Path II, as shown in Figure 6; that is:

$$\begin{aligned} \Phi_1 &= \{b_1, c_1, b_4\} \\ \Phi_2 &= \{b_2, c_1, b_5\} \\ \Phi_3 &= \{b_3, b_6\} \\ \Phi_4 &= \phi \\ \Phi_5 &= \phi \\ \Phi_6 &= \phi \end{aligned} \tag{10}$$

The actual search process is based on dynamic programming [1, 12], where the local cost function is defined in the next section. The dynamic programming algorithm is essentially a multi-stage optimization technique where at each stage, or each iteration, the size of the path is increased by one set of feature segments. In this context, each hypothesis contributes to a number of possible configuration of boundary segments. Each configuration then activates neighboring hypotheses for construction of new configurations subject to mutual exclusion. This process continues until all boundary segments are processed. The best path for a given set of configuration is then recovered by searching for minimum error. This process is then repeated for each "starting" hypothesis, and configuration with the least amount of error is then selected as the optimum segmentation. In this fashion, local, adjacency, and global consistency is met. Formally, let P be a set of states, D be a set of possible decisions, $F: P \times D \mapsto \mathcal{F}$ be a cost function, and $\psi: P \times D \mapsto P$ be a function that maps the current state and a decision into the next state. In a single step, the minimum possible value starting from state p_i is given by $H_1(p_i) = \min_{d \in D} F(p_i, d)$. By the same token, choosing a decision d that minimizes the value of a sequence for n states starting from p_i is found by:

$$H_n(p_i) = \min_{d \in D} [F(p_i, d) + H_{n-1}(\psi(p_i, d))] \tag{11}$$

The above recurrence relation, together with the cost function, specifies an optimum path for a desired configuration.

3.3 Evaluation criteria

Although nuclei may have completely different morphology, we have some general information about their shapes and properties. This information enables us to compare different hyperquadrics, get rid of the undesirable ones, and reduce false alarms. The "goodness" criterion includes four terms: area A, shape S, overlap O, and error C. Each criterion is evaluated by its representative function E_A, E_S, E_O, and E_C. The cost of the local hyperquadric is then given by $E_T = E_A + E_S + E_O + E_C$. The cost of one path is the summation of costs of the entire set of hypotheses. The transition cost between two adjacent hypotheses is simply an exclusive consistency measure. E_A, E_S, E_O and E_C are computed as follows:

1. E_A. A is the area of the hyperquadric. A nucleus should neither be bigger than (A_b) nor smaller than (A_s).

$$E_A = \begin{cases} 0, & \text{if } A_s \leq A \leq A_b \\ 1 - e^{-\frac{A - A_b}{\sigma_A}} & \text{if } A > A_b \\ 1 - e^{-\frac{A_s - A}{\sigma_A}} & \text{if } A < A_s \end{cases} \tag{12}$$

where we choose $A_b = L^2, A_s = \frac{1}{4}L^2$.

2. E_S. S is defined as an aspect ratio as measured by the ratio of minor to major axes as shown in Figure 7(a). E_S is defined to favor perfect circles:

$$E_S = 1 - e^{-\frac{1-S}{\sigma_S}} \tag{13}$$

3. E_O. A hyperquadric may not always be enclosed by the nuclei clump. An overlap measure is defined as the ratio of area inside the clump to the total area of the hyperquadric. E_O is defined to favor larger values of O as shown in Figure 7(b):

$$E_O = 1 - e^{-\frac{1-O}{\sigma_O}} \tag{14}$$

4. E_C. The error C is defined as $C = \frac{\epsilon^2}{m}$, where ϵ is the error in (5) of the hyperquadric fitting process and m is the total number of points:

$$E_C = 1 - e^{-\frac{C}{\sigma_C}} \tag{15}$$

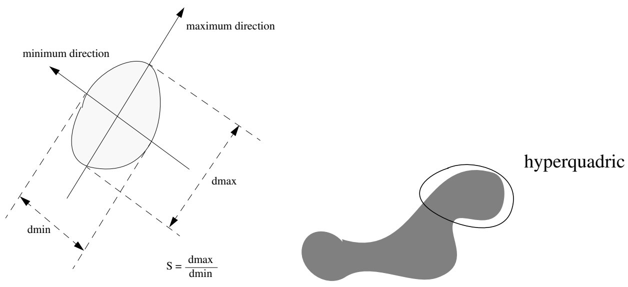

(a) (b)

Figure 7: Evaluation criteria. (a) shape rate; (b)overlap rate.

$\sigma_A, \sigma_S, \sigma_O, and\ \sigma_C$ are weighting factors for each criterion.

3.4 Post-processing

Two kinds of error may occur in the fitting process: a fit that spans outside of the clumped boundary (background inclusion) and a fit that encloses other nuclei as well. The first error is resolved through a simple "AND" operation. The second error is the result of the overlap of two or more adjacent hyperquadrics representation, as shown in Figure 8. Here, we utilize a simple model to express the dynamic behavior of the boundary, as shown in Figure 9(a). Let two elastic contours $\mathcal{C}_1, \mathcal{C}_2$ be squeezed against each other. The stable boundary between them will be affected by the rebound force that corresponds to the energy of deformation. The rebound force $\mathcal{F}$ at any point on the deformed contour is proportional to its displacement d from the original position and perpendicular to the new boundary, as shown in Figure 9(b), $\mathcal{F} = \alpha d$. The deformation energy is given by $e = \int_L \frac{1}{2}\beta d^2 ds$, where α, β are elastic parameters. At equilibrium, $\mathcal{F}_1 = \mathcal{F}_2$ along L and the deformation energy should be minimum, as shown in Figure 9(c). Then it is not difficult to prove that every point on L must have the same distance from its original positions on $\mathcal{C}_1$ and $\mathcal{C}_2$.

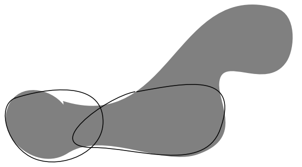

Figure 8: Error due to overlap between two neighboring hyperquadrics.

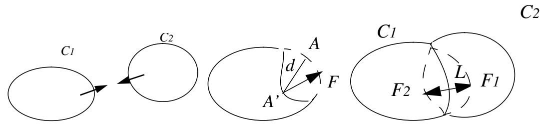

(a) (b) (c)

Figure 9: Contour dynamic: (a) two contours are squeezed together; (b) contour dynamic; (c) stable state.

We use a protocol based on distance transform to partition squeezed hyperquadrics. Let region $\mathcal{R}$ contain h hyperquadrics $h_i, i = 1, ..., h$ with some overlap where the distance transformations, $\mathcal{D}_i(x, y)$, for each hyperquadric is computed. Then each point $(x, y) \in \mathcal{R}$ is assigned to ith nucleus if $\mathcal{D}_i(x, y) \geq \mathcal{D}_j(x, y), \forall j = 1, ..., h,\ (x, y)$, as shown in Figure 10(a)(b).

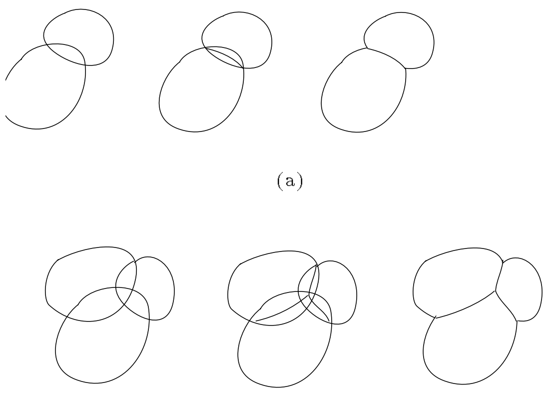

(a)

(b)

Figure 10: Steps in resolving the overlap problem between multiple nuclei: (a) two nuclei; (b) three nuclei.

4 Experimental results

The proposed segmentation technique has been tested on real data obtained through a fluorescent imaging microscope. The results computed by our approach as well as the "correct" segmentations generated manually by skilled operator interaction are presented in Figures 11 through 15. Comparisons between the two types of results are summarized in table 4. A more detailed analysis of the different types of error made by our system is shown in table 4.

Table 1. Performance of the Proposed Technique

Index	Ground Truth	Our method	Rejected
11	10	7	3
12	11	7	4
13	4	4	0
14	12	9	3
15	14	12	2

.

Table 2. Types of Error in the Proposed Technique

Index	Boundary	Fused	Split	Correct	Accuracy
11	1	0	0	6	88
12	1	0	0	6	88
13	0	0	0	4	100
14	0	1	1	7	77
15	1	1	0	10	83

"Boundary" indicates the numbers of nuclei with incorrect partial boundary locations; "Fused" indicates the numbers of nuclei that are merged together; "Split" indicates the numbers of nuclei that are fragmented into two or more small shapes; "Correct" indicates the number of nuclei correctly detected by our algorithm; and "Accuracy" corresponds to the percentages of acceptable nuclei to detected ones. As we can see, the nuclei lying on the boundaries of the original images are rejected, since most of their boundary segments can not be provided. In Figure 14, one nucleus is fragmented into two small shapes because of the false crease information. The absence of crease segment as well as the fact that, in some situations, a bigger nucleus is "better" than two very small ones (according to our criteria), leads to the fusion of nuclei in Figures 14 and 15. "Boundary" error happens in Figures 11, 12, 15 because the boundary information is not strong enough to accentuate concave corners. Since our approach seeks a global solution, it is possible that local incorrect segmentation is a penalty for a lower global error.

In all of our experiments, the hyperquadric has four terms, $N = 4$. The evaluation parameters are $L = 45$, $\sigma_A = 200$, $\sigma_S = 5$, $\sigma_O = 0.5$, and $\sigma_C = 1$. These numbers are obtained based on empirical knowledge of the specific application domain.

5 Conclusion

We have presented a new approach for segmentation of nuclei based on partial geometric information. Two key issues are hyperquadric fitting and assignment matrix. Hyperquadric representation can model a broad range of shapes from partial boundary information. The assignment matrix, on the other hand, converts the segmentation problem into a constrained optimization problem. Our approach aims for global consistency, and as a result, it is less error prone, generating a fewer false alarms for final verification by an operator. Our current research focuses on 3D segmentation of 3D confocal data set.

Acknowledgments: Authors thank Dr. Mary Helen Barcellos-Hoff and Mr. Sylvain Costes for motivating the problems, valuable discussion, and providing the data used in this experiment.

References

[1] A. Amini, T. Weymouth, and R. Jain. Using dynamic programming for solving variational problems in vision. *IEEE Transactions on Pattern Analysis and Machine Intelligence*, pages 855–867, 1990.

[2] S. Han, D. Goldgof, and K. Bowyer. Using hyperquadric for shape recovery from rane data. In *Proceedings of the IEEE International Conference on Computer Vision*, pages 292–296, 1993.

[3] A. Hanson. Hyperquadrics: smoothly deformable shapes with convex polyhedral bounds. *Computer Vision, Graphics, and Image Processing*, 44:191–210, 1988.

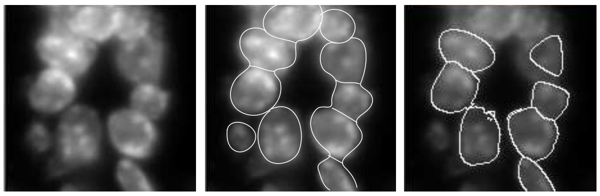

(a) (b) (c)

Figure 11: Segmentation results: (a) original image; (b) correct segmentation; (c) our segmented nuclei.

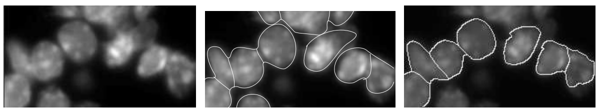

(a) (b) (c)

Figure 12: Segmentation results: (a) original image; (b) correct segmentation; (c) our segmented nuclei.

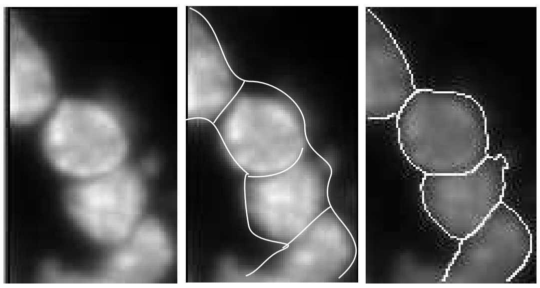

(a) (b) (c)

Figure 13: Segmentation results: (a) original image; (b) correct segmentation; (c) our segmented nuclei.

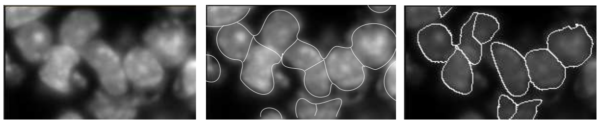

(a) (b) (c)

Figure 14: Segmentation results: (a) original image; (b) correct segmentation; (c) our segmented nuclei.

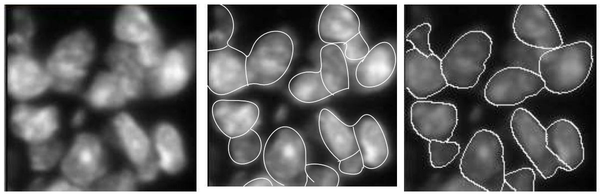

(a) (b) (c)

Figure 15: Segmentation results: (a) original image; (b) correct segmentation; (c) our segmented nuclei.

[4] Y. Jin, Jayasooriah, and R. Sinniah. Clump splitting through concavity analysis. *Pattern Recognition*, 15:1013–1018, 1994.

[5] S. Kumar, S. Han, D. Goldgof, and K. Boeyer. On recovering hyperquadrics from range data. *IEEE Transactions on Pattern Analysis and Machine Intelligence*, 17(11):1079–1083, 1995.

[6] J. Leu and H. Yau. Detection of the dislocations in metal crystals from microscopic images. *Pattern Recognition*, 24(1):41–56, 1991.

[7] J. Liang. Intelligent splitting the chromosome domain. *Pattern Recognition*, 22:519–532, 1989.

[8] O. Monga, N. Ayache, and P. Sander. From voxel to intrinsic surface features. *Image and Vision Computing*, 10(6), 1992.

[9] O. Monga, S. Benayoun, and O. Faugeras. From partial derivatives of 3d density images to ridge lines. In *Proceedings of the Conference on Computer Vision and Pattern Recognition*, pages 354–359, 1992.

[10] S. Ong, H. Yeow, and R. Sinniah. Decomposition of digital clumps into convex parts by contour tracing and labelling. *Pattern Recognition Letters*, 13:789–795, 1992.

[11] W. Press, S. Teukollsky, W. Vetterling, and B. Flannery. *Numerical Recipes in C*. Cambridge Unvi. Press, 1992.

[12] Bellman R. *Dynamic Programming*. Princeton University Press, 1957.

[13] P. Saint-Marc, J. Chen, and G. Medioni. Adaptive smoothing: A general tool for early vision. *IEEE Transactions on Pattern Analysis and Machine Intelligence*, 13(6):514–530, 1991.

[14] M. Sonka, V. Hlavac, and R. Boyle. *Image Processing analysis and Machine Vision*. Chapman & Hall, 1995.

[15] D. Struik. *Lectures on classical differential geometry*. Dover Publications, New York, 1988.

[16] H. Talbot and I Villalobos. Binary image segmentation using weighted skeletons. *SPIE Image algebra and morphological image processing*, 1769:393–403, 1992.

[17] J. Thirion. New feature points based on geometric invariants for 3d image registration. *International Journal of Computer Vision*, 18(2):121–137, 1996.

[18] J. Thirion and A. Gourdon. The 3d matching lines algorithm. *Graphical Models and Image Processing*, 58(6):503–509, 1996.

[19] W. Wang. Banary image segmentation of aggregates based on polygonal approximation and classification of concavities. *Pattern Recognition*, 31(10):1502–1524, 1998.